

Excitation of Rainfall over the Tropical Western Pacific

YANPING LI

International Pacific Research Center, University of Hawaii at Manoa, Honolulu, Hawaii

R. E. CARBONE

National Center for Atmospheric Research, Boulder, Colorado*

(Manuscript received 21 September 2011, in final form 25 April 2012)

ABSTRACT

The authors have examined 4 years of satellite-derived SST and rainfall data in anticipation of a relationship between SST structure and the excitation of convective rainfall. The results exhibit a strong excitation signal consistent with the presence of mesoscale SST gradients in about 75% of approximately 10 000 rainfall onset events. Rainfall onset events occur at locations with enhanced horizontal convergence, as inferred by the Laplacian of SST on scales of order 100 km. The daily SST field exhibits multiscale patchiness, spanning a 2+°C range. The signal is disproportionately large at SSTs that are 0.25°C above the mean, near 29.5°C; disproportionately weak for SST \leq 28.8°C; and proportionately neutral for SST \geq 30.3°C. The calculations suggest that a characteristic strength of this lower-boundary forcing ($\sim 3 \times 10^{-5} \text{ s}^{-1}$) is approximately one order of magnitude stronger than the mean regional background forcing ($\sim 3 \times 10^{-6} \text{ s}^{-1}$). The periphery of warm oceanic patches exhibits both convergent and divergent Laplacian values of similar frequency and magnitude; however, rainfall onset favors the locally convergent locations by a 3:1 ratio.

1. Introduction

The objective of this study is to explore the role of daily sea surface temperature (SST) structure in relation to the excitation of convective rainfall over the tropical western Pacific warm pool. With few exceptions this problem has been approached as a regional-scale background forcing that scales with SST. However, for the 4-yr period of record, the correlation between SST and cumulative rainfall is only 0.42 in boreal summer, when convective rainfall events are most frequent. Largely overlooked is the potential significance of mesoscale solenoidal circulations as a deterministic mechanism for excitation of oceanic rainfall events. Below, we briefly discuss analogous forcings over continents, tropical islands, and western boundary current regions,

followed by a selective summary of literature directly relevant to Pacific warm pool conditions.

a. Background

It is well known that lower-boundary forcing is one of the most influential factors governing the occurrence of deep moist convection and related precipitation. Elevated heat sources such as mountains (e.g., Tripoli and Cotton 1989), heterogeneous terrain (e.g., Whiteman 1990), and sea breezes (e.g., Simpson 1994) are known to trigger continental warm-season rainfall events. These events often organize, scale upward, and spread rainfall to regions well beyond preferred genesis zones (e.g., Carbone et al. 2002; Laing et al. 2008; Wang et al. 2004; Levizzani et al. 2006; Pereira Filho et al. 2010; Keenan and Carbone 2008). Associated with genesis, horizontal gradients or “boundaries” of temperature and moisture are often the result of antecedent convection, topographic influences, or differential diurnal heating resulting from soil moisture or land cover (e.g., Wilson and Schreiber 1986; Segal and Arritt 1992). These gradients induce upward air motion as part of solenoidal circulations (Tripoli and Cotton 1989; Carbone et al. 2002), thereby deepening the atmospheric boundary

* The National Center for Atmospheric Research is sponsored by the National Science Foundation.

Corresponding author address: Yanping Li, P.O. Box 3000, Boulder, CO 80301.
E-mail: yanping@ucar.edu

layer and effecting a reduction of convective inhibition (CIN).

Similar processes are active over tropical islands in the absence of significant topography (e.g., Keenan et al. 1994; Wilson et al. 2001). Slow surface flow over islands of order 100 km can result in deepening and moistening of the island boundary layer along a trajectory from windward to leeward shores, where sea breeze convergence preferentially triggers deep convection. In the event of a lower-tropospheric flow reversal, winds aloft can steer leeward-triggered storms over the energized island boundary layer (Carbone et al. 2000).

Large-scale atmospheric low-level convergence can be determined by the absolute value of local SST (Neelin and Held 1987). Deep convective heating becomes especially intense when SST approaches about 28°C (Gadgil et al. 1984; Fu et al. 1994; Ramanathan and Collins 1991). Large-scale SST gradients (SSTGs) are more important than local SST maxima in determining regional-scale ascent in the marine atmospheric boundary layer (Lindzen and Nigam 1987; Back and Bretherton 2009) when accompanied by large-scale ascent aloft. The Lindzen and Nigam mechanism was focused on response to large-scale SST features with weak gradients, where the air remained in equilibrium with SST and advection could be ignored.

Most mesoscale studies have focused on the response to boundary layer anomalies, often in association with subtropical/midlatitude western boundary currents. In such regions, the mesoscale convergence has been attributed to feedback from SST gradients, as discussed by Chelton et al. (2004), Minobe et al. (2008), Small et al. (2008), and Xie (2004). Elevated SST and quasi-stationary SST gradients locally modify the atmospheric boundary layer and decrease deep tropospheric stability, thereby triggering and/or amplifying precipitation in these regions (Minobe et al. 2008; Xie 2004). Atmospheric pressure adjustments to these sharp SST gradients lead to surface wind convergence, which anchors a narrow band of precipitation along the Gulf Stream. In the absence of influence from transient synoptic disturbances, much of the convection is quasi-stationary over the local SST anomaly, failing to travel as free convection with the ambient tropospheric winds.

b. Focus of this study

The western Pacific warm pool region is characterized by an atmosphere with low CIN, substantial convective available potential energy (CAPE), weak-to-moderate easterly shear, and favorable large-scale forcing owing to its location with respect to the Hadley and Walker circulations (e.g., Johnson and Ciesielski 2000; Lau and Sui 1997; Raymond 1995). Annually, the ocean surface

layer spans 27°–31°C and is often quite shallow and stable. Upper-ocean stability is attributed to a regular supply of freshwater at the surface, which can be further stabilized by cumulative diurnal warming from incident shortwave radiation. This combination of ocean–atmosphere conditions is conducive to strong coupling, for example, as observed and modeled in research related to the Tropical Ocean and Global Atmosphere Coupled Ocean–Atmosphere Response Experiment (TOGA COARE) (Webster and Lukas 1992).

Rainfall is frequent and copious over the western Pacific warm pool, in part because of periodic enhanced forcing by regional-scale transient disturbances. Disturbances include equatorial Rossby waves, equatorially trapped Kelvin waves, westward-propagating inertio-gravity waves, and westerly wind bursts, sometimes associated with disturbances of midlatitude origin in boreal winter (Kiladis et al. 2009). In general, there is a mean zonal confluence of energetic air in the lower troposphere, fueled primarily by latent heat fluxes at the ocean surface.

Since soundings in this region typically offer little inhibition to deep convection, the atmosphere is vulnerable to relatively weak excitation mechanisms, which, upon casual inspection, may appear to be quasi-random. This is somewhat analogous to the evolution in our understanding of midsummer continental convection. So-called airmass convection is an amusing tall tale of mid-twentieth-century meteorology in light of deterministic processes, now known to be responsible for convective initiation in weakly forced conditions (e.g., Wilson and Schreiber 1986). Similar representations of tropical oceanic convection are likely incomplete and may contribute to marked deficiencies in global climate model performance (Back and Bretherton 2009).

A basic objective of this investigation is to determine, by means of physical/statistical analyses of observations and the application of existing theory, whether or not transient mesoscale SST gradients influence the time and location of rainfall excitation. The domain of choice (Fig. 1) for this investigation was selected for the very low fraction of island landmass, the potential seasonal variations induced by the Northern Hemisphere winter, and the general quality and accessibility of satellite data.

Section 2 describes the observations and computational procedures. Section 3 presents the SST morphology and derivatives thereof, together with statistics related to the onset of rainfall events. Section 4 evaluates the strength of mesoscale lower-boundary forcing in light of rainfall onset statistics and coincident properties of the SST field. Section 5 summarizes the conclusions and discusses avenues for future research.

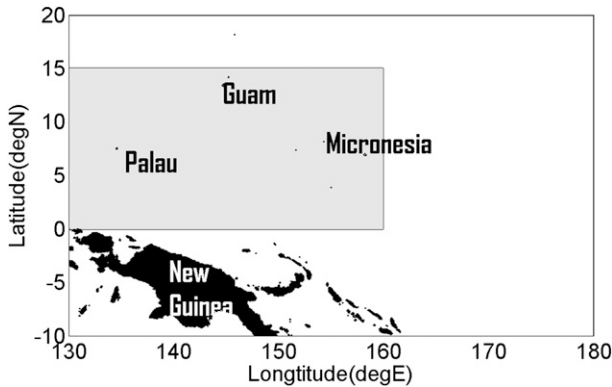


FIG. 1. Computational domain (shaded).

2. Observations and computation

We mainly rely on two satellite composite datasets: those of the Climate Prediction Center (CPC) morphing technique (CMORPH) for time-resolved rainfall estimates and the Group for High-Resolution Sea Surface Temperature (GHRSSST) for the daily averaged SST field. We also examined Quick Scatterometer (QuikSCAT) winds for supporting evidence of surface convergence along with interim European Centre for Medium-Range Weather Forecasts (ECMWF) Re-Analysis (ERA-Interim) and National Centers for Environmental Prediction (NCEP)–National Center for Atmospheric Research (NCAR) reanalysis data for the background meteorological fields.

a. Rainfall data (CMORPH; Joyce et al. 2004)

CMORPH produces global precipitation analyses at high spatial and temporal resolution. The estimation technique relies exclusively on quantitative precipitation estimates that have been derived from low-orbit satellite microwave observations, the features of which are temporally interpolated and advected from geostationary satellite IR data [Multifunctional Transport Satellite (MTSAT) data in this instance]. Here, we utilize the CMORPH data beginning April 2006, with a spatial resolution of 0.25° and 3-h temporal resolution.

To examine the relationship between onset of convective rainfall and the local SST pattern, we have developed an algorithm for the determination of event onset time and location. The algorithm is based on that of Carbone et al. (2002), where it was applied exclusively in reduced dimension analyses. For this study, the algorithm has been extended to two horizontal dimensions. More than 10 000 rainfall onset events were identified over the 4-yr period of record, about 7 day^{-1} . Details are provided in appendix A.

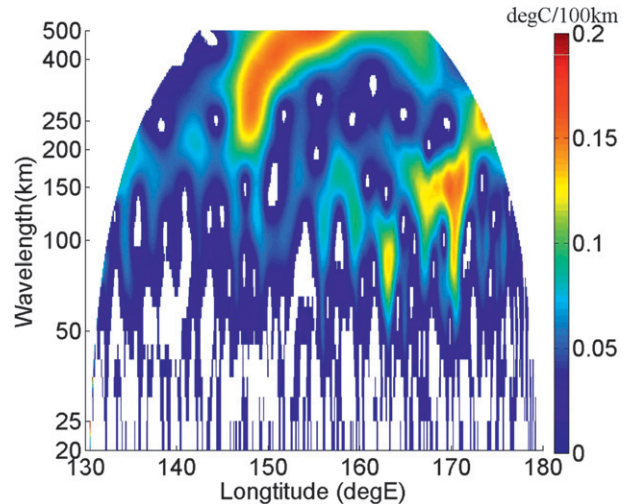


FIG. 2. Wavelet analysis for GHRSSST on 19 Jul 2009 at 5°N . SST variation at wavelengths $< 150 \text{ km}$ is damped as a result of a dominant $\sim 25\text{-km}$ microwave footprint in the merged product. SST gradient zones may be characterized as half wavelength, thereby capturing a substantial fraction of true amplitude for scales $\geq 75 \text{ km}$.

b. SST data (GHRSSST; Donlon et al. 2007)

GHRSSST is an internationally produced dataset consisting of daily averages on a 5-km grid. Both microwave and infrared data are assimilated, as appropriate for conditions. The sources include the National Oceanic and Atmospheric Administration (NOAA) series of Advanced Very High Resolution Radiometer (AVHRR) polar-orbiting satellites, NOAA series of Geostationary Orbiting Environmental Satellites (GOES), NASA's Moderate Resolution Imaging Spectroradiometer (MODIS) instrument on board the *Terra* and *Aqua* earth satellites, the European Advanced Along-Track Scanning Radiometer (AATSR) onboard the *Envisat* satellite, the European Geostationary Spinning Enhanced Visible Infrared Imager (SEVIRI) onboard Meteosat, the Tropical Rainfall Measuring Mission (TRMM) Microwave Imager (TMI), the Advanced Microwave Radiometer–Earth Observing System (AMSR-E), and the Japan Aerospace Exploration Agency's (JAXA's) MTSAT. The advantage of this dataset is that it is quality controlled by international experts and relatively small-scale SSTGs can be resolved, especially under clear-sky conditions (Donlon et al. 2007). The realizable spatial resolution from GHRSSST is dynamic, being dependent upon cloudiness.

A wavelet analysis (Fig. 2) for one sample day of SST shows that approximately 5% of the energy is associated with resolved SSTGs at wavelengths $< 50 \text{ km}$, monotonically increasing to 35% at 200–400 km. SSTGs

observed by research vessels in this region are known to be as large as $2^{\circ}\text{C} (3 \text{ km})^{-1}$ (Soloviev and Lukas 1996), well below resolvable scales with GHRSSST under ordinary cloud cover conditions. Such SSTGs are approximately one order of magnitude sharper, with amplitude 3 times greater, than the SSTGs presented in section 3. Based on inspection of selected wavelet analyses, we assume that harmonic content of GHRSSST in our (relatively cloudy) domain is often limited to that which microwave sensor footprint dimensions (20–25 km) permit. Therefore, we estimate that more than 50% of the true SSTG amplitude is reliably passed at the 75-km half-wavelength scale from GHRSSST data, given that theory predicts recovery of about 75% true amplitude if the waveform is resolved from five independent point measurements per wavelength.

We employ polynomial curve fitting to calculate SSTG and the Laplacian of SST (LSST) simultaneously. This method utilizes information from the surrounding pixels while significantly decreasing the impact of pseudorandom errors at one specific location. The polynomial function has a highest order up to 10. The moving window for the curve fit is 20 grid points ($\sim 1^{\circ}$ lat/lon). The calculated SSG/LSST is smoothed within five grid points ($\sim 25 \text{ km}$). The polynomial function order and the window width were tested and selected to best resolve the mesoscale gradients present. Technical details of the polynomial curve fitting method are given in appendix B.

3. SST morphology and lower-boundary forcing

a. SST climatology and daily variability: Relationship to rainfall onset location

SST seasonal climatologies for the 4-yr period of record are illustrated in Figs. 3 and 4. For boreal summer [June–August (JJA); Fig. 3a], the SST field is smooth, with minima 29.1° – 29.3°C and maxima 29.5° – 29.9°C . As expected, the seasonal mean exhibits a relatively large-scale pattern, whereas daily SST fields routinely exhibit multiple scales of variability that span a larger dynamic range. For example, the SST distribution on a typical boreal summer day (Fig. 3b) exhibits a relatively large dynamic range (28.7° – 30.7°C). The locations of rainfall onset for this day (black diamonds) are shown to occur over a relatively wide range of SST.

In boreal winter, the December–February (DJF) average SST field (Fig. 4a) exhibits properties similar to JJA. A significant difference between summer and winter is that SST decreases monotonically northward, from 29.3° to 27.5°C . Because of the seasonal tendency toward cooler SST northward of 10°N , a zonal alignment of SST patterns is often evident, together with large-amplitude mesoscale substructure at all orientations. For example, a DJF daily

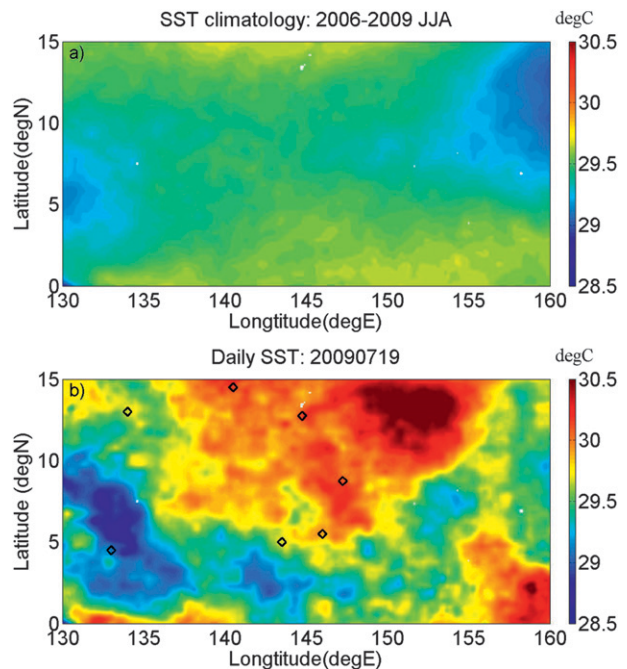


FIG. 3. (a) SST climatology: 4-yr average for JJA. (b) SST daily reality: 19 Jul 2009. Daily SST areas and gradients thereof are multiscale and extend over a larger dynamic range. Rainfall onset locations are marked (black diamonds). Note wide range of SST at onset.

SST field (Fig. 4b) is similar to JJA both in its multiscale properties and in the dynamic range of SST, extending to cooler (26.5°C) values in the northeast sector. The locations of rainfall onset for this day (black diamonds) are shown to occur over a relatively wide range of SST.

The 4-yr distribution of SST at the points of rainfall onset (Fig. 5, red) reveals systematic behavior relative to the background distribution of SST (Fig. 5, black). The peak ratio of rainfall onset to background SST occurs near the modes of both distributions, dropping below unity for $\text{SST} \leq 28.9^{\circ}\text{C}$ and to unity at the warmest SST locations ($\geq 30.3^{\circ}\text{C}$). Here, unity implies an SST value that is neither favored nor disfavored with respect to the background SST field. On the day following rainfall onset (Fig. 5, blue), the SST, at the original onset locations, decreases slightly (0.15°C). We speculate that this is a response to the rain itself and convectively driven winds.

b. SST gradient morphology

Gradients of SST are ubiquitous within the domain for the entire period of record. Example SSTG fields (associated with SST in Figs. 3b, 4b) are shown in Figs. 6a,b for 19 July 2009 and 10 February 2007, respectively. As in Figs. 3b and 4b, rainfall onset locations are marked by black diamonds. The gradients in Figs. 6 exhibit multiscale structure and amplitude variations consistent with the parent SST fields. Especially in boreal winter

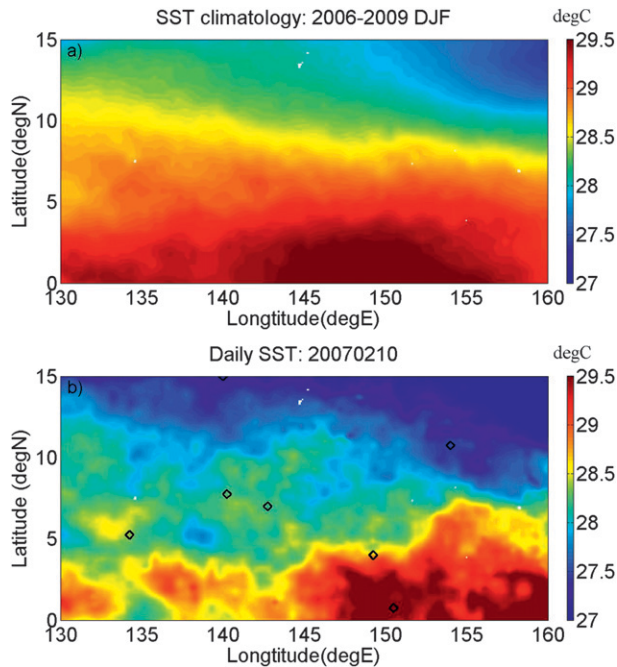


FIG. 4. (a) SST climatology: 4-yr average for DJF. (b) SST daily reality: 10 Feb 2007. Daily SST areas and gradients thereof are multiscale and extend over a larger dynamic range. Rainfall onset locations are marked (black diamonds). Note wide range of SST at onset.

(Fig. 6b), a tendency toward larger-scale zonal alignment is evident, together with imbedded mesoscale substructure at various orientations. A de facto upper limit of SSTG [$\sim 1^{\circ}\text{C} (1^{\circ}\text{lat/lon})^{-1}$] is largely determined by the spatial scales passed in the GHRSSST product under cloudy conditions, as previously discussed in section 2. Smaller-scale gradients, where present, are partially or fully attenuated. Occasionally, larger-amplitude mesoscale gradients are observed, presumably under suppressed conditions, where geostationary IR data have been widely assimilated.

Time rate of change within the gradient field primarily spans the period from daily to weekly. It is common for a few percent of the SST/SSTG anomalies to markedly change in 1 or 2 days. Individual gradients assume various forms including open quasilinear filaments, partial or completely closed rings, and irregular closed shapes. Conceptually, these would be consistent with frontlike boundaries bordering or enclosing the edges of warm/cool/saline/freshwater patches. Hints of gradual expansion or contraction of some closed gradients are occasionally evident; however, it is more common for gradients to simply amplify or dissipate on a time scale of one to several days. Also observed is coherent SSTG amplification or dissipation in sizeable subregions of the domain, the cause for which is a subject of further study.

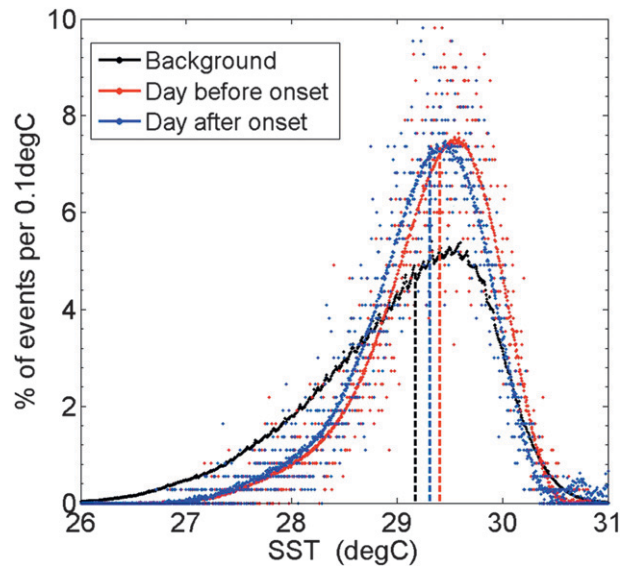


FIG. 5. 4-yr distribution of rainfall onset SST (red), post-rainfall onset SST (blue), and oceanic background SST (black). Mean onset SST is $\sim 0.25^{\circ}\text{C}$ warmer than the background mean. Overall, onset occurrence is disproportionately concentrated in mid-SST range. The warmest SST areas are proportionately neutral with respect to frequency of onset. SST decreases $\sim 0.15^{\circ}\text{C}$ at the original onset locations on the day following onset.

c. Gradient orientation

The 4-yr distribution of background ocean gradient orientation (black) is shown in Fig. 7. Distance from the origin is proportional to percentage of occurrences. Also shown (red) is the percentage of occurrences of gradient orientation at all 10 000 rainfall onset locations. In an absolute sense the preferred direction is southward-directed (toward warm) gradients, followed by westward, eastward, and northward. In a relative sense, per unit ocean surface, rainfall onset is preferred on eastward-directed gradients. In an east (west) wind this would be the leeward (windward) shore of a warm patch. In a relative sense, southward-directed gradients are disfavored locations despite the fact that their numbers are large. Given that mean winds in the region are primarily zonal, this suggests a longitudinal (approximately gradient-parallel) flow relationship to meridional gradients. As previously mentioned, seasonality of the SST field leads to extensive southward-directed SST gradients in boreal winter.

d. Atmospheric surface convergence

Under slow mean flow, lower-boundary thermal gradients can induce horizontal hydrostatic pressure gradients, the spatial variation of which defines a horizontal divergence field in the atmospheric boundary layer. Such pressure gradients induce downgradient flow on a local scale, which is largely unaffected by rotational

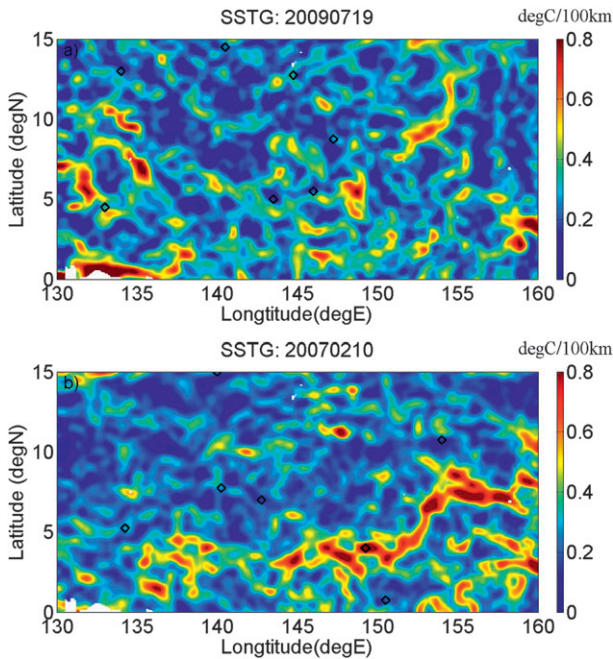


FIG. 6. SST gradient field: (a) July example; (b) February example. Note cellular structure throughout and mesoscale structure within larger-scale gradient in February.

effects in near-equatorial regions. Divergence is given by the Laplacian of SST: $Div_t = (\bar{p}_b g H / \bar{T}_b) \times LSST$. LSST may be qualitatively described as the “curvature” of SSTG. While gradients vary greatly in their shape, the tendency is toward a divergent curvature near gradient base (concave upward) and convergent above the mid-gradient temperature (convex upward). Example LSST fields are shown in Fig. 8 as calculated for the boreal summer and winter days previously used to illustrate SST and SSTG in Figs. 3b, 4b, and 6a,b. The LSST fields are cellular in character on scales of 50–200 km. A dipole structure is clearly evident, reflecting curvature of opposite sign between the lower and upper portions of gradients. The negative pole (yellow to red) is convergent. From Fig. 8 it is clear that such forcing is present throughout the domain but with considerable variability in amplitude and scale. As previously, rainfall onset locations are shown, the majority of which in these examples are coincident with convergent values, $-LSST$. While these examples appear to agree with our working hypothesis, 14 excitations from a population of 10 000 does not speak to whether such forcing is routinely associated with rainfall excitation, a principal aim of this study.

We assume that statistical inferences of significance and a potential causal relationship should satisfy at least two criteria:

- 1) There is a disproportionate spatial/temporal coincidence of moist convection excitation associated with

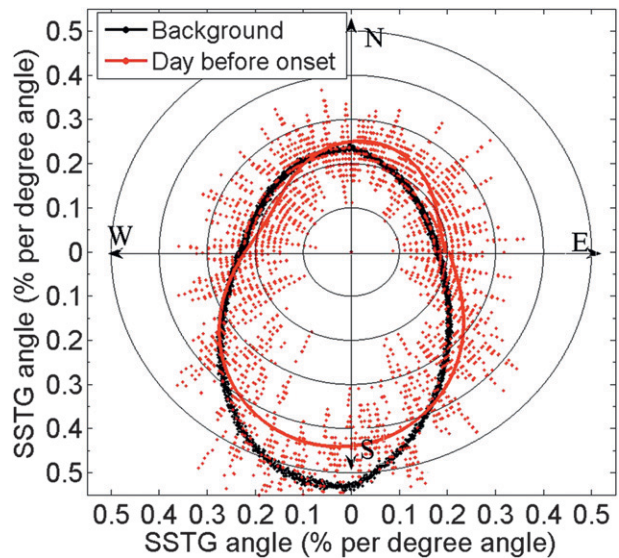


FIG. 7. 4-yr background SST orientation distribution (black) and rainfall onset orientation distribution (red). The relative phase change suggests that onset is less favored at southward-pointing SSTG and preferred at eastward-pointing SSTG (western side of warm anomaly in westerly flow). See text for additional explanation.

this forcing compared to its occurrence in the broader background ocean.

- 2) The characteristic magnitude of local LSST forcing markedly exceeds that of large-scale forcing.

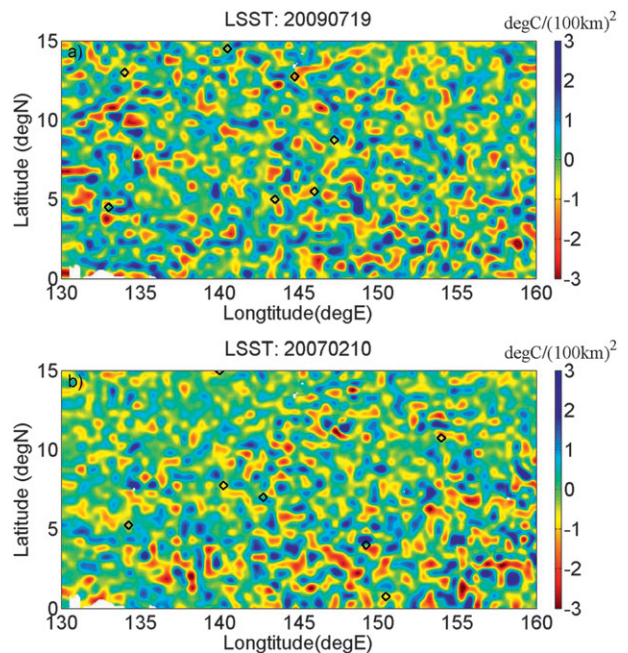


FIG. 8. Examples of LSST field and precipitation onset locations (black diamonds): (a) July example; (b) February example. Positive values connote likely locations of enhanced atmospheric horizontal convergence near the lower boundary. See text for explanation.

In answer to statement 1, we have compiled statistics for approximately 10 000 events to address the spatial/temporal coincidence issue and have compared this to the background ocean condition.

In answer to statement 2, we have performed a quantitative analysis of induced surface convergence based on governing theory, the observed LSST properties, and calculations to estimate the atmospheric response under low mean flow, all of which are presented in section 4.

e. Coincidence of LSST with rainfall onset

We have examined the statistical relationship between the onset of rainfall and LSST on the days prior to and following the onset of each rainfall event, of which there are approximately 10 000. Events near $LSST = 0$, where sign could not be determined within 3σ uncertainty, have been expunged from Fig. 9 for clarity. The prior-day LSST distribution is shown as a function of SST in Fig. 9a. Rainfall onset statistics show a majority of events ($\sim 75\%$) with convergent (i.e., negative) values of LSST. Nearly all of the events originate between 28.2° and 30.2°C with a maximum frequency near 29.5°C . The day following onset (Fig. 9b), the distribution shifts toward the divergent side of LSST, where about 60% of the prior-day event excitation locations are now divergent. Nearly all of the divergent locations are between 28.2° and 30.0°C . The set of prior and post-rainfall onset statistics are kinematically and thermodynamically consistent with expected changes in forcing and the SST.

Figure 10 shows the onset data from Fig. 9 as LSST probability density functions, together with the probability density function of background LSST. As in Fig. 9, about 75% of onset events occur at convergent values of LSST distribution (red), decreasing to about 40% convergent thereafter (blue). Most important is the ratio of background LSST (black) to rainfall onset frequency and the depletion of convergent LSST following rainfall onset. The pre-onset ratio is maximized near $LSST = -0.7^\circ\text{C} (100 \text{ km}^2)^{-1}$. Post onset, the depletion of convergent locations is at moderate to large negative LSST values. By definition, this result is fully consistent with rainfall excitation at the strongest lower-boundary forcing locations. When these LSST statistics are considered together with SST onset statistics (Fig. 5), the results are consistent with rainfall onset at the periphery of warm SST anomalies [i.e., where curvature of SSTG may be maximized and SST is modestly (0.25°C) above average]. Statistically, the highest SST locations have relatively neutral LSST. The relationships revealed here may be among the reasons why rainfall amount is often locally uncorrelated with maximum SST, while also significantly correlated with elevated SST over larger regions on an annual time scale.

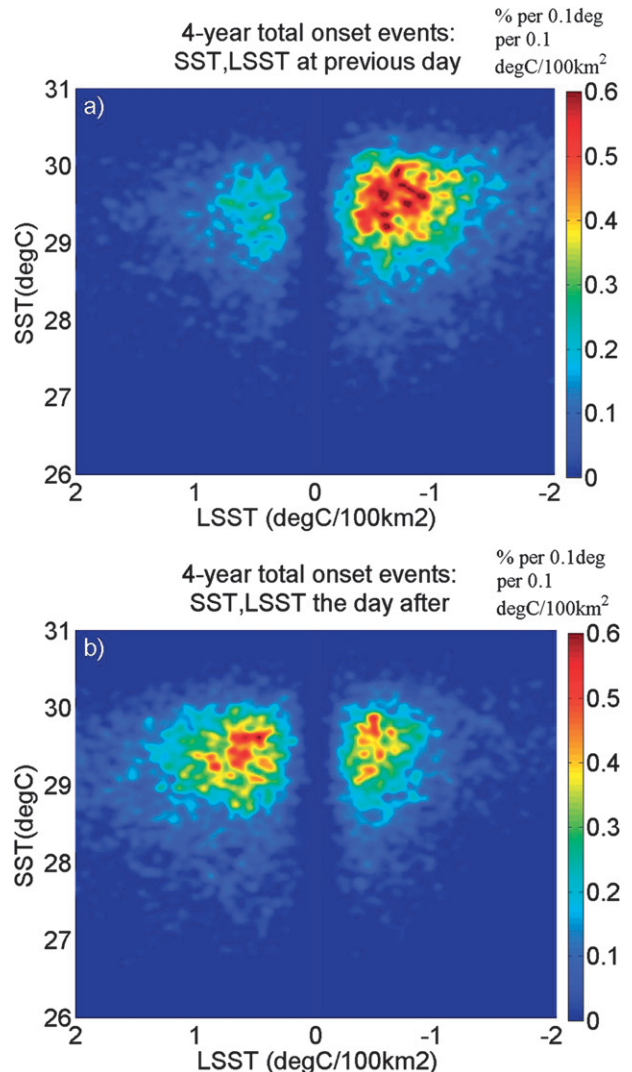


FIG. 9. SST and LSST distribution before and after onset events: (a) previous day; (b) following day. As expected, there is a large shift from convergent to divergent curvature of LSST.

4. Analysis and discussion

Section 3 provided statistical evidence of SSTG/LSST forcing that appears strong enough to influence the time and location of rainfall onset. We have performed calculations, based on governing theory and characteristics of the observed SST structure, to determine if local forcing is potentially of sufficient strength to modulate large-scale forcing. Large-scale forcing in this region, as analyzed by ERA-Interim, NCEP-NCAR reanalysis, and QuikSCAT winds, all point to a regional average of about $3 \times 10^{-6} \text{ s}^{-1}$.

We approach the local-scale problem from two complementary perspectives, a breeze approximation and a gravity current approximation, which share similar

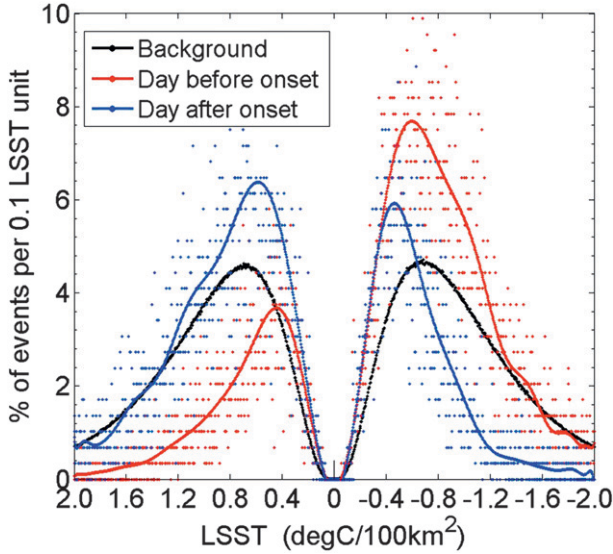


FIG. 10. Same data as in Fig. 9, illustrating the before and after onset shift in relation to background LSST. The shift represents approximately a factor of 2 from background frequency in each phase. Note the post-onset depletion of most moderate- to large-magnitude negative LSST values.

attributes in the presence of a lower-boundary gradient. The breeze formulation may be thought of as the “pull” of the heat source, and the gravity current formulation may be thought of as the “push” of a surrounding cold pool. Both of these thermally direct circulations are commonplace throughout the world, admittedly in somewhat different settings than applied here.

a. Breeze approximation

Our method for estimating the surface convergence caused by SST gradients requires two assumptions. Prior to onset, we assume that the mesoscale temperature and pressure gradients are small above the top of the mixed layer. We also assume that the shallow mixed layer above the sea surface satisfies both the hydrostatic assumption and the Boussinesq approximation for air motions induced by local pressure/temperature gradients.

The pressure perturbation within a thin layer dz is

$$dp'(z) = \rho'(z) g dz. \quad (1)$$

According to the perfect gas law $p(z) = \rho(z)RT(z)$, with $p'(z)/p_b(z) \approx \rho'(z)/\rho_b(z) + T'(z)/T_b(z)$. The subscript b (i.e., basic) denotes the environmental mean, with $p(z) = p_b(z) + p'(z)$.

In general, for the western Pacific warm pool region, $p'(z)/p_b(z) \sim 0.5 \times 10^{-3}$ and $T'(z)/T_b(z) \sim 2 \times 10^{-3}$, as estimated from the amplitude of diurnal variation in TOGA COARE surface data. Therefore, we assume $\rho'(z)/\rho_b(z) \approx -T'(z)/T_b(z)$.

Substituting $\rho'(z)$ into Eq. (1), we get

$$dp'(z) \approx -\rho_b(z) g \frac{T'(z)}{T_b(z)} dz \quad (2)$$

and

$$\begin{aligned} p'(z=0) &\approx -\int_{z=0}^{z=H} \rho_b(z) g \frac{T'(z)}{T_b(z)} dz \\ &\approx -\frac{\bar{\rho}_b g}{\bar{T}_b} \times T'(z=0) \times H, \end{aligned} \quad (3)$$

where $z = H$ is the top of the mixed layer. According to soundings from TOGA COARE (Johnson et al. 2001), potential temperature is nearly constant below 925 hPa, so we estimate $H = 700$ m. Here $\bar{\rho}_b$ and \bar{T}_b are the environmental mean air density and air temperature, respectively.

Given the Boussinesq approximation, and ignoring the background mean wind and Coriolis effect, the momentum equations become

$$u_t = -p'_x/\bar{\rho}_b, \quad (4)$$

$$v_t = -p'_y/\bar{\rho}_b. \quad (5)$$

The convergence is $-(u_x + v_y) = w_z$, so the time derivative of surface convergence becomes

$$\begin{aligned} -(u_x + v_y)_t = w_{zt} &= \frac{p'_{xx} + p'_{yy}}{\bar{\rho}_b} = -\frac{gH}{\bar{T}_b} (T'_{xx} + T'_{yy}) \\ &= -\frac{gH}{\bar{T}_b} \times \text{LSST}. \end{aligned} \quad (6)$$

While the diurnal variation of SST can be substantial, we assume the diurnal variation of LSST is relatively small. Additionally, we assume that both SSTG and LSST diminish in magnitude linearly as a function of increasing height by introducing an effective depth H_e of 350 m. This permits a conservative estimate of lower-boundary forcing that is consistent with boundary layer observations in related phenomena, such as atmospheric gravity currents.

Then, the surface convergence associated with the local SSTG becomes

$$-(u_x + v_y) = w_z = -\frac{gH_e}{\bar{T}_b} \times \text{LSST}_m \times \Delta t \quad (7)$$

where Δt is defined as a characteristic transport time across the warm patch and LSST is replaced with its daily mean LSST_m . From Fig. 9, the median of $-\text{LSST}_m$ is approximately $0.6^\circ\text{C} (100 \text{ km}^2)^{-1}$. Consistent with the 100-km scale, we assume cylindrical symmetry for the warm patch with radius $R = 50$ km. Then the associated

surface convergence (Con) is defined by a mean radial convergence velocity $v_{\text{rm}} = R/2 \times \text{Con} = R/\Delta t$, assuming the convergent flow spans the roughly 100-km warm patch (~ 50 -km radial transport). From Eq. (7), we know that $\text{Con} = [(9.8 \times 350)/300] \times (0.6/10^{10}) \times \Delta t$, so then $\Delta t = 5.4 \times 10^4$ s, $v_{\text{rm}} = 0.93$ m s $^{-1}$, and

$$\text{Con} \approx \frac{9.8 \times 350}{300} \times \frac{0.6}{(10^5)^2} \times (5.4 \times 10^4) \approx 3.7 \times 10^{-5} \text{ s}^{-1}.$$

b. Gravity current approximation

An alternative approach is to consider convergence to be a consequence of gravity/density current propagation in a quasi-steady state.

- 1) For a 2D gravity current, $v = \sqrt{kgH_e(\Delta T/T)}$, assuming $H_e = 350$ m, and $\Delta T \sim 0.3^\circ\text{C}$ [given that $-\text{LSST}_m$ is approximately 0.6°C (100 km^2) $^{-1}$]. For $k = 1$, $v = \sqrt{1 \times 9.8 \times 350 \times (0.3/300)} \sim 1.8$ m s $^{-1}$. Then

$$\text{Con} = \frac{dv}{dx} = \frac{1.8}{50 \times 10^3} = 3.6 \times 10^{-5} \text{ s}^{-1}.$$

- 2) For cylindrical symmetry analogous to a warm “island” surrounded by cooler waters and converging air,

$$\begin{aligned} \text{Con} &= \frac{\partial v}{\partial x} = \frac{1}{A} \times \frac{\partial A}{\partial t} = \frac{1}{\pi R^2} \times 2\pi R v_r \\ &= \frac{2v_r}{R} \sim \frac{2 \times 1.8}{50 \times 10^3} = 7 \times 10^{-5} \text{ s}^{-1}, \end{aligned}$$

which is twice that for both linear gravity current symmetry and the gravity wave approximation. While arguable, it may be appropriate to view the atmospheric boundary layer density structure as a “sea” of weak density currents (i.e., sharper transition zones than resolvable by GHRSSST data), since flow is relatively balanced and constant for a finite but indefinite period.

NCEP global reanalyses suggest that periods of strong large-scale forcing, associated with transient disturbances, may be comparable in magnitude to our calculations of local SSTG forcing. Such periods may favor the majority of rainfall events that experience onset when LSST is neutral or positive.

c. QuikSCAT divergence

We attempted to use the divergent component of QuikSCAT winds to improve or verify our theory-based calculations at the 50–100-km scale. We expect the divergent component of wind to be about 1 m s $^{-1}$. According to Schlax et al. (2001), QuikSCAT winds, when sampled over 3° and 12 days, have an uncertainty of about 1 m s $^{-1}$ provided the wind speed exceeds about 2 m s $^{-1}$

(Ebuchi et al. 2002). Our requirement is daily data owing to the expected, and statistically verified, reversal in sign of LSST. Nevertheless, we calculated daily divergence from QuikSCAT winds at rainfall onset locations and found the divergent component to be noiselike. The comparison with a subset of LSST-calculated divergence at onset locations revealed a modest measure of agreement in the sign of divergence for about 60% of the onset events.

d. Spatial relationship of rainfall onset to warm SST patches

The preferred range of SST for rainfall onset (Fig. 5) suggests a preference for off-center onset locations in relation to a warm patch. Off-center locations can be located on the windward, leeward, or a longitudinal “shore” of a warm patch, generally in proximity to an LSST maximum, and, because of its curvature, at a somewhat diminished SSTG amplitude. An examination of the onset data, together with QuikSCAT regional wind direction, suggests that surface winds are mainly weak easterly (westerly) when excitation occurs over an eastward (westward)-directed gradient. This implies a leeward shore excitation in both instances.

The leeward location is thermodynamically advantageous in the sense that flow across the full extent of a warm patch deepens and moistens the atmospheric boundary layer, lowering convective inhibition. Since the surface wind is most often westerly, together with easterly flow aloft, there exists a critical level in most instances. In the case of leeward shore excitation with a critical level, mid-to-upper-level steering winds enable deep convection to traverse the warm patch, thus providing the potential for heavier rainfall early in an event life cycle. This regime was consistently observed in the Tiwi Islands (Carbone et al. 2000) as discussed in section 1.

Since the mean regional flow is almost always zonal, it will usually have a longitudinal (roll) relationship to a warm patch on its zonally oriented flanks. We do not have adequate information to infer a preferred zonal wind direction associated with onset along a zonally oriented shore. However, we note that a boreal winter southward-directed SSTG prevails, which can lead to a high frequency of “north shore” events.

Figure 11 provides idealized illustrations of potential spatial relationships among a warm patch, surface and steering winds, lower-boundary convergence, onset of rainfall, and the movement of convective storms. It should be emphasized that these relationships are statistically inferred and are not directly observed. They are thermodynamically and kinematically consistent with similar phenomena observed elsewhere and available governing theory.

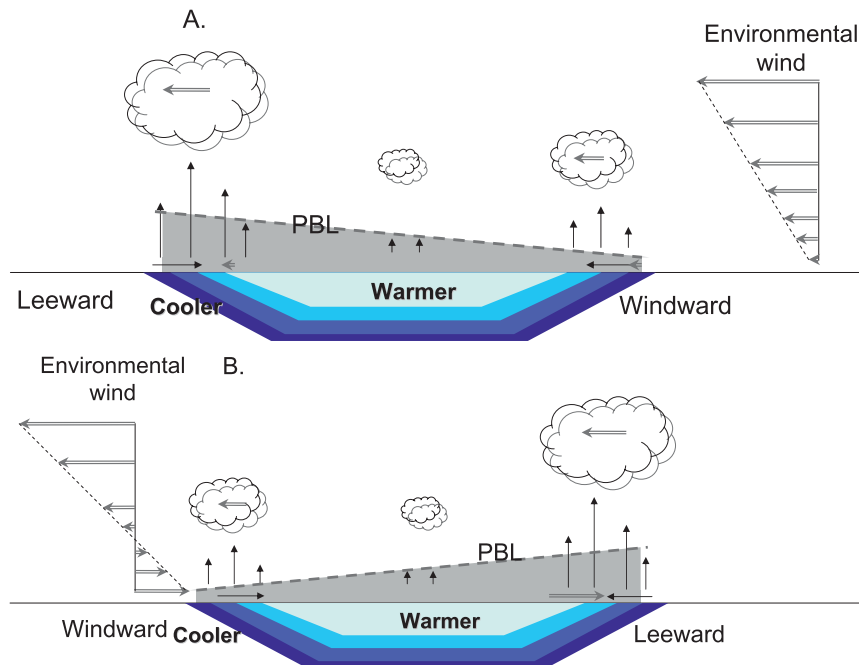


FIG. 11. Schematic representation of wind profiles and favored rainfall onset locations over a hypothetical oceanic warm patch, based on convergence at the lower boundary.

5. Conclusions and future work

The analyses of SST structure and precipitation events in the tropical western Pacific reveal a disproportionate coincidence between mesoscale SST gradient zones and the onset of rainfall events. Our related findings are as follows:

- The region of study is regularly and highly populated with mesoscale SST gradients, which are resolved in our analysis at the 50–200-km range.
- Approximately 75% of rainfall onset events are spatially and temporally coincident with a maximum of local surface convergence, as estimated from the Laplacian of SST.
- The Laplacian-derived local convergence is about $3\text{--}7 \times 10^{-5} \text{ s}^{-1}$, which is approximately one order of magnitude larger than regional background convergence ($\sim 3 \times 10^{-6} \text{ s}^{-1}$). We regard this result, together with the observed onset statistics, as persuasive evidence of forcing sufficient to excite deep moist convection.
- The combined statistics of SST gradients together with local QuikSCAT winds suggest a preference for rainfall onset on the leeward “shore” of a warm water patch. In the case of westerly surface winds with easterlies aloft, circumstances are especially favorable to rapid development of heavy precipitation.

We speculate that rainfall and local, convectively generated, winds are likely a principal source of the observed SST gradients. Future research should investigate this

ocean–atmosphere coupling in greater detail, including the potential for coherent regeneration/excitation of rainfall that could arise from organized convective systems (e.g., Chen and Houze 1997; Zhang 2005). Future investigations should also seek to obtain a more complete understanding of local diurnal convection, and any amplification or dissipation effects associated with SST gradients and the excitation of convection. The evolution of SST structure under suppressed conditions is among those of particular interest, including the oceanic capacity to accumulate daily residuals of energy, potentially leading to periodic cycles of convective rainfall.

Acknowledgments. This research was supported by the Japan Agency for Marine–Earth Science and Technology (JAMSTEC), by NASA through Grant NNX07AG53G, and by NOAA through Grant NA09OAR4320075, which sponsor research at the International Pacific Research Center. The authors gratefully acknowledge Tom Schroeder and Mark Merrifield, directors of the Joint Institute for Marine and Atmospheric Sciences (JIMAR), for their encouragement and assistance in support of local travel expenses and publication page charges (National Oceanic and Atmospheric Administration Grant NA09OAR4320075). Roger Lukas provided valuable insights about ocean surface structure during the conduct of this study. Gary Barnes provided a much appreciated informal review. Thanks are due to two anonymous reviewers, who curbed

our excesses and gave us hope that QuikSCAT winds could be helpful in the analysis. Any opinions, findings, conclusions, or recommendations expressed in this publication are those of the authors and do not necessarily reflect the views of the National Science Foundation.

APPENDIX A

Algorithm to Detect the Onset of and to Track Sustained Rainfall Events

This algorithm is developed based on the reduced dimension technique of Carbone et al. (2002). Here we extend the technique by restoring the second horizontal dimension as follows:

- 1) The entire computational domain is searched for conterminous patches of precipitation at time t . A Gaussian function is fit to each feature:

$$\begin{aligned} & \text{RainAmount}(x, y; x_0, y_0) \\ &= A(x_0, y_0) \exp \left[-\frac{(x - x_0)^2}{R_x(x_0, y_0)} - \frac{(y - y_0)^2}{R_y(x_0, y_0)} \right] + \varepsilon. \end{aligned}$$

- For each position (x_0, y_0) , a least squares fit determines $A(x_0, y_0)$, $R_x(x_0, y_0)$, and $R_y(x_0, y_0)$. The autocorrelation $\sigma(x_0, y_0)$ between precipitation data and the Gaussian fit is calculated within the range $(x_0 \pm R_x, y_0 \pm R_y)$.
- 2) For precipitation data at time t , search the local maximum for $\sigma(x, y)$ with the condition $\sigma(x, y) > 0.50$ and $A(x, y) > 1.0$.
- 3) Compare the fields of precipitation data at time t and $t + 1$. A new precipitation center $(x, y, t + 1)$ is tagged either as the new center position of an ongoing event or the onset position of a new event. The threshold between these is within about 200 km (8 pixels), which is consistent with the observed upper limit of convective system propagation speed (18.5 m s^{-1}). In this way, we can trace the propagation of the precipitation centers, since each continuous event has a unique assigned number upon onset detection.
- 4) The total precipitation amount associated with a single event is defined as the summation of the precipitation along its path within the radius of an ellipse circumscribing the precipitation center:

$$\text{TotalRainAmount} = \sum_{t=t\text{start}}^{t=t\text{end}} \sum_{x=x_0(t)-R_x[x_0(t),y_0(t),t]}^{x=x_0(t)+R_x[x_0(t),y_0(t),t]} \sum_{y=y_0(t)-R_y[x_0(t),y_0(t),t]}^{y=y_0(t)+R_y[x_0(t),y_0(t),t]} \text{Rain}(x, y, t).$$

APPENDIX B

Polynomial Curve Fit Method for Calculation of SSTG and LSST

For SST at a specific position (x_0, y_0) , the surrounding pixels SST(x, y_0) can be written as a distance x function:

$$\begin{aligned} \text{SST}(x, y_0) \approx & C_p(x - x_0)^p + C_{p-1}(x - x_0)^{p-1} \\ & + \dots + C_2(x - x_0)^2 \\ & + C_1(x - x_0)^1 + C_0. \end{aligned} \quad (\text{B1})$$

Similarly, the surrounding pixels SST(x_0, y) can be written as a distance y function

$$\begin{aligned} \text{SST}(x_0, y) \approx & D_p(y - y_0)^p + D_{p-1}(y - y_0)^{p-1} \\ & + \dots + D_2(y - y_0)^2 \\ & + D_1(y - y_0)^1 + D_0. \end{aligned} \quad (\text{B2})$$

We find the coefficients of a polynomial [the right-hand side of Eqs. (B1) and (B2)] of degree p that fits SST(x, y_0) and SST(x_0, y) in a least squares sense. If x represents the west–east direction and y represents the south–north direction, the longitudinal gradient of SST at position (x_0, y_0) is $[\partial \text{SST}(x, y_0) / \partial x]_{x=x_0} = C_1$. The Laplacian of SST at position (x_0, y_0) is $[\partial^2 \text{SST}(x, y_0) / \partial x^2]_{x=x_0} = 2C_2$. The amplitude and direction of SST gradient at position (x_0, y_0) in two dimensions becomes the absolute value and the angle of the complex $C_1 + iD_1$. The magnitude of the Laplacian of SST at position (x_0, y_0) in two dimensions becomes $2(C_2 + D_2)$.

The principal advantage of this curve-fitting method is the utilization of information in the surrounding pixels, significantly decreasing the effect of isolated errors compared with finite-differencing methods. For example, the standard deviation of the SST retrieval is about 0.3°C over the western Pacific. The error bar of the calculated $-\text{LSST}$ (Figs. 7, 8) is about 0.05°C (100 km^2) $^{-1}$ if using a polynomial fit of order $p = 10$, window = 20 pixels, and a smoothing of 5 pixels. We have performed sensitivity tests for polynomials of

different order, different windows (as small as 20 pixels or as large as 100 pixels), and different smoothing ranges. The results shown here are quite robust, the major effect being diminished amplitude with increased smoothing. The overall structure is nearly identical. A larger window with lower polynomial order passes synoptic scales of variation at the expense of mesoscale gradients.

REFERENCES

- Back, L. E., and C. S. Bretherton, 2009: On the relationship between SST gradients, boundary layer winds, and convergence over the tropical oceans. *J. Climate*, **22**, 4182–4196.
- Carbone, R. E., J. W. Wilson, T. D. Keenan, and J. M. Hacker, 2000: Tropical island convection in the absence of significant topography. Part I: Life cycle of diurnally forced convection. *Mon. Wea. Rev.*, **128**, 3459–3480.
- , J. D. Tuttle, D. A. Ahijevych, and S. B. Trier, 2002: Inferences of predictability associated with warm season precipitation episodes. *J. Atmos. Sci.*, **59**, 2033–2056.
- Chelton, D. B., M. G. Schlax, M. H. Freilich, and R. F. Milliff, 2004: Satellite measurements reveal persistent small-scale features in ocean winds. *Science*, **303**, 978–983.
- Chen, S. S., and R. A. Houze Jr., 1997: Diurnal variation and life cycle of deep convective systems over the tropical Pacific warm pool. *Quart. J. Roy. Meteor. Soc.*, **123**, 357–388.
- Donlon, C., and Coauthors, 2007: The Global Ocean Data Assimilation Experiment High-Resolution Sea Surface Temperature Pilot Project. *Bull. Amer. Meteor. Soc.*, **88**, 1197–1213.
- Ebuchi, N., H. C. Graber, and M. J. Caruso, 2002: Evaluation of wind vectors observed by QuikSCAT/SeaWinds using ocean buoy data. *J. Atmos. Oceanic Technol.*, **19**, 2049–2062.
- Fu, R., A. D. Del Genio, and W. B. Rossow, 1994: Influence of ocean surface conditions on atmospheric vertical thermodynamic structure and deep convection. *J. Climate*, **7**, 1092–1108.
- Gadgil, S., V. Joseph, and N. V. Joshi, 1984: Ocean–atmosphere coupling over monsoon regions. *Nature*, **312**, 141–143.
- Johnson, R. H., and P. E. Ciesielski, 2000: Rainfall and radiative heating rates from TOGA COARE atmospheric budgets. *J. Atmos. Sci.*, **57**, 1497–1514.
- , —, and J. A. Cotturone, 2001: Multiscale variability of the atmospheric mixed layer over the western Pacific warm pool. *J. Atmos. Sci.*, **58**, 2729–2750.
- Joyce, R. J., J. E. Janowiak, P. A. Arkin, and P. Xie, 2004: CMORPH: A method that produces global precipitation estimates from passive microwave and infrared data at high spatial and temporal resolution. *J. Hydrometeorol.*, **5**, 487–503.
- Keenan, T. D., and R. E. Carbone, 2008: Propagation and diurnal evolution of warm season cloudiness in the Australian and Maritime Continent region. *Mon. Wea. Rev.*, **136**, 973–994.
- , B. Ferrier, and J. Simpson, 1994: Development and structure of a Maritime Continent thunderstorm. *Meteor. Atmos. Phys.*, **53**, 185–222.
- Kiladis, G. N., M. C. Wheeler, P. T. Haertel, K. H. Straub, and P. E. Roundy, 2009: Convectively coupled equatorial waves. *Rev. Geophys.*, **47**, RG2003, doi:10.1029/2008RG000266.
- Laing, A. G., R. E. Carbone, V. Levizzani, and J. D. Tuttle, 2008: The propagation and diurnal cycles of deep convection in northern tropical Africa. *Quart. J. Roy. Meteor. Soc.*, **134**, 93–109.
- Lau, K.-M., and C. H. Sui, 1997: Mechanisms of short-term sea surface temperature regulation: Observations during TOGA COARE. *J. Climate*, **10**, 465–472.
- Levizzani, V., R. Ginetti, A. G. Laing, and R. E. Carbone, 2006: Warm season precipitation climatology: First European results. *Adv. Geosci.*, **7**, 15–18.
- Lindzen, R. S., and R. S. Nigam, 1987: On the role of sea surface temperature gradients in forcing low-level winds and convergence in the tropics. *J. Atmos. Sci.*, **44**, 2418–2436.
- Minobe, S., A. Kuwano-Yoshida, N. Komori, S.-P. Xie, and R. J. Small, 2008: Influence of the Gulf Stream on the troposphere. *Nature*, **452**, 206–209.
- Neelin, J. D., and I. M. Held, 1987: Modeling tropical convergence based on the moist static energy budget. *Mon. Wea. Rev.*, **115**, 3–12.
- Pereira Filho, A. J., R. E. Carbone, J. E. Janowiak, P. Arkin, R. Joyce, R. Hallak, and C. G. M. Ramos, 2010: Satellite rainfall estimates over South America—Possible applicability to the water management of large watersheds. *J. Amer. Water Resour. Assoc.*, **46**, 344–360.
- Ramanathan, V., and W. Collins, 1991: Thermodynamic regulation of ocean warming by cirrus clouds deduced from observations of the 1987 El Niño. *Nature*, **351**, 27–32.
- Raymond, D. J., 1995: Regulation of moist convection over the west Pacific warm pool. *J. Atmos. Sci.*, **52**, 3945–3959.
- Schlax, M. G., D. B. Chelton, and M. H. Freilich, 2001: Sampling errors in wind fields constructed from single and tandem scatterometer datasets. *J. Atmos. Oceanic Technol.*, **18**, 1014–1036.
- Segal, M., and R. W. Arritt, 1992: Nonclassical mesoscale circulations caused by surface sensible heat-flux gradients. *Bull. Amer. Meteor. Soc.*, **73**, 1593–1604.
- Simpson, J. E., 1994: *Sea Breeze and Local Winds*. Cambridge University Press, 234 pp.
- Small, R. J., and Coauthors, 2008: Air–sea interaction over ocean fronts and eddies. *Dyn. Atmos. Oceans*, **45**, 274–319.
- Soloviev, A., and R. Lukas, 1996: Observation of spatial variability of diurnal thermocline and rain-formed halocline in the western Pacific warm pool. *J. Phys. Oceanogr.*, **26**, 2529–2538.
- Tripoli, G. J., and W. R. Cotton, 1989: Numerical study of an observed orogenic mesoscale convective system. Part I: Simulated genesis and comparison with observations. *Mon. Wea. Rev.*, **117**, 273–304.
- Wang, C.-C., G. T.-J. Chen, and R. E. Carbone, 2004: A climatology of warm season cloud patterns over East Asia based on GMS infrared brightness temperature observations. *Mon. Wea. Rev.*, **132**, 1606–1629.
- Webster, P. J., and R. Lukas, 1992: TOGA COARE: The Coupled Ocean–Atmosphere Response Experiment. *Bull. Amer. Meteor. Soc.*, **73**, 1377–1416.
- Whiteman, C. D., 1990: Observations of thermally developed wind systems in mountainous terrain. *Atmospheric Processes over Complex Terrain, Meteor. Monogr.*, No. 45, Amer. Meteor. Soc., 5–42.
- Wilson, J. W., and W. E. Schreiber, 1986: Initiation of convective storms at radar-observed boundary-layer convergence lines. *Mon. Wea. Rev.*, **114**, 2516–2536.
- , R. E. Carbone, J. D. Tuttle, and T. D. Keenan, 2001: Tropical island convection in the absence of significant topography. Part II: Nowcasting storm evolution. *Mon. Wea. Rev.*, **129**, 1637–1655.
- Xie, S.-P., 2004: Satellite observations of cool ocean–atmosphere interaction. *Bull. Amer. Meteor. Soc.*, **85**, 195–208.
- Zhang, C., 2005: The Madden–Julian oscillation. *Rev. Geophys.*, **43**, RG2003, doi:10.1029/2004RG000158.